# On strain hardening mechanism in gradient nanostructures

CrossMark

Jianjun Li [a, b, *], G.J. Weng [c], Shaohua Chen [d], Xiaolei Wu [e]

[a] Department of Engineering Mechanics, School of Mechanics, Civil Engineering and Architecture, Northwestern Polytechnical University, Xi'an 710129, Shaanxi, China
[b] Department of Microstructure Physics and Alloy Design, Max-Planck-Institut für Eisenforschung GmbH, Düsseldorf 40237, Germany
[c] Department of Mechanical & Aerospace Engineering, Rutgers University, New Brunswick, NJ 08903, United States
[d] Institute of Advanced Structure Technology, Beijing Institute of Technology, Beijing 100081, China
[e] State Key Laboratory of Nonlinear Mechanics, Institute of Mechanics, Chinese Academy of Sciences, Beijing 100190, China

## ARTICLE INFO

## ABSTRACT

Experiments have shown that a gradient design, in which grain size spans over four orders of magnitude, can make strong nanomaterials ductile. The enhanced ductility is attributed to the considerable strain hardening capability obtained in the gradient metals. A non-uniform deformation on the lateral sample surface is also observed. This might inject geometrically necessary dislocations (GNDs) into the sample. However, no direct evidence has been provided. Therefore the issues remain: why can the gradient structure generate high strain hardening, and how does it reconcile the strength-ductility synergy of gradient nanostructures? Here for the first time we quantitatively investigate the strain hardening of a gradient interstitial-free steel by developing a dislocation density-based continuum plasticity model, in which the interaction of the component layers in the gradient structure is represented by incorporating GNDs and back stress. It is demonstrated that both the surface non-uniform deformation and the strain-hardening rate up-turn can be quantitatively well predicted. The results also show that the strain hardening rate of the gradient sample can reach as high as that of the coarse-grained counterpart. A strength-ductility map is then plotted, which clearly show that the gradient samples perform much more superior to their homogeneous counterparts in strength-ductility synergy. The predicted map has been verified by a series of experimental data. A detailed analysis on GNDs distribution and back stress evolution at the end further substantiates our view that the good strain hardening capability results from the generation of abundant GNDs by the surface non-uniform deformation into the nano-grained layers of the gradient sample.

## 1. Introduction

Refining grains down to nanoscale renders metals ultra-high strength but low ductility (Beyerlein et al., 2015; Farrokh and Khan, 2009; Gleiter, 1989; Khan et al., 2000; Khan and Liu, 2016; Li et al., 2014; Meyers et al., 2006; Ovid'ko, 2002; Rodríguez-Galán et al., 2015; Rupert, 2016; Weng, 2011; Zhu and Li, 2010). The ultra-high strength opens a new challenge of reconciling both strength and ductility in nanostructured metallic metals and alloys. This strength-ductility trade-off dilemma has led to

a severe setback to their engineering applications. Therefore, over the last two decades it has been constantly pursued to have the unity of nano-grain's ultra-high strength and coarse-grain (CG)'s excellent ductility in the same sample (Kou et al., 2014; Li et al., 2010b ; Li et al., 2016; Liu et al., 2015; Lu et al., 2009; Ma, 2006; Ovid'ko and Langdon, 2012; Wang et al., 2002; Wei et al., 2014; Youssef et al., 2005; Zhao et al., 2008). Recently, gradient nanostructured metals have attracted much interests due to their high strength and high ductility (Fang et al., 2011; Kou et al., 2014; Li and Soh, 2012a; Lu, 2014; Moering et al., 2015, 2016; Wu et al., 2014a; Yang et al., 2016; Yin et al., 2016; Yuan et al., 2016; Zeng et al., 2016). For example, a gradient copper made by surface mechanical grinding treatment possesses almost the same uniform tensile elongation and a doubled yield strength as compared with its CG counterpart (Fang et al., 2011).

This class of materials is marked by a gradual grain-size variation from the sample surface into its interior by four orders of magnitude. As shown in Fig. 1a and b, the grain size in the gradient structure is typically tens of nanometers on the surface layer, but deep in the sample it can increase to the CG size (typically tens of micrometers). This is in sharp contrast to those homogeneous samples with uniform grain size distribution (Fig. 1c). Generally, the gradient structure has two gradient surface layers (one on the top and the other at the bottom), and in-between a sandwiched CG core (Fig. 2a). This type of microstructures can be produced by surface nano-crystallization technique, which has been introduced in the form of many process variations that are both cost-effective and amenable to large-scale industrial production, such as surface mechanical attrition treatment (Lu and Lu, 2004) and surface mechanical grinding treatment (Li et al., 2008).

The good balance of strength and ductility of gradient sample is found to be resulted from the considerable strain hardening capability obtained in the gradient structure (Wu et al., 2014a; Yang et al., 2015). For example, a strain hardening up-turn is observed in the gradient interstitial free (IF) steel sample fabricated by Wu et al. (2014a) using surface mechanical attrition treatment. The up-turn, also found in copper (Yang et al., 2015), is believed to be responsible for the high strength and ductility in the gradient IF steel sample, i.e., 2.5 times higher yield strength at a loss of only 3.3% uniform elongation as compared with the CG counterpart. They also observed a non-uniform deformation on the lateral surface of the gradient sample with a height profile up to 30 μm that is absent in ordinary homogeneous structures (Fig. 2). The non-uniform deformation might generate geometrically necessary dislocations (GNDs) into the gradient sample but no evidence has been provided.

As compared with so many experimental investigations, corresponding simulation and theoretical works are scarce due to the huge grain size variation in the gradient structure. All the existing crystal plasticity and molecular dynamics studies are limited to 2-D structures, in which the grain size varies only across two length scales (~10 nm−~100 nm) (Li et al., 2015b; Liu and Mishnaevsky Jr., 2014; Zeng et al., 2016), because of the high computational cost, whereas the theoretical investigations tend to focus on 1-D stress state without incorporating the interface effect of different layers (Li et al., 2010a; Li and Soh, 2012b). Although one could get some insights from the above investigations, they cannot describe the 3-D nature of the problem with the experimentally observed lateral surface non-uniform deformation. Therefore, there are several critical questions remained to be answered: (1) what leads to the strong strain hardening in the gradient structure? (2) how does the non-uniform deformation form on the lateral surface? (3) are the GNDs that are associated with the surface non-uniform deformation responsible for the strong strain hardening capability? (4) if the answer of (3) is yes, what is their quantitative relation? and (5) how does the gradient microstructure modulate the strain hardening? In order to answer the above critical questions, we embark on the development of a dislocation density-based theoretical model to quantitatively describe the strain hardening in gradient structure. Since non-uniform deformation is generally associated with GNDs (Ashby, 1970; Demir et al., 2009; Fleck and Hutchinson, 1993; Gao et al., 1999; Lyu et al., 2015; Martínez-Pañeda and Niordson, 2016), it is important to incorporate the effect of GNDs in the present model.

The paper is organized as follows. The developed model will be presented in Section 2 to identify the constitutive behavior of all the component layers by considering GNDs and back stress. The overall mechanical response is then calculated based on
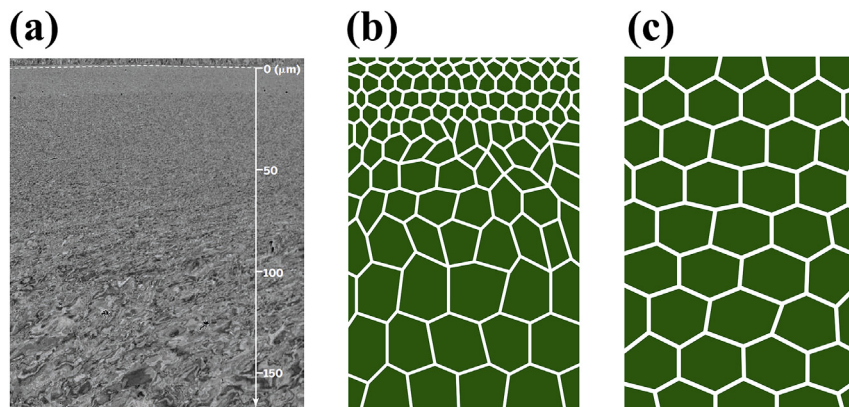


**Fig. 1.** (a) Microstructure of gradient sample, reprinted from Lu (2014) with permission from AAAS, and (b) its schematic diagram. (c) Schematic of homogeneous structure.
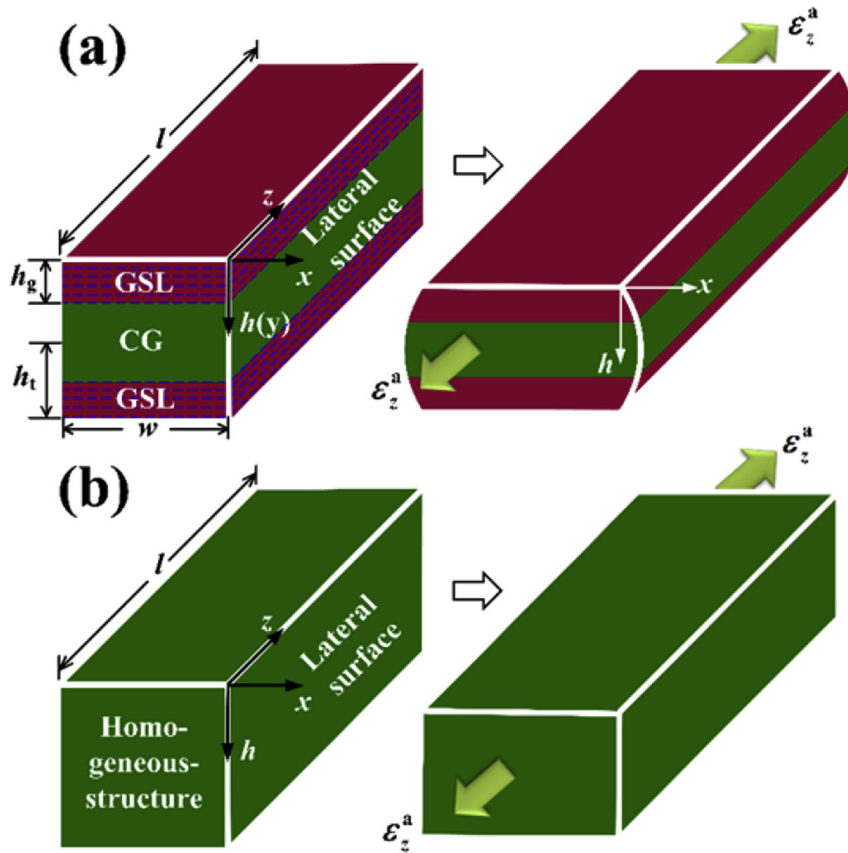
**Fig. 2.** Schematic diagram of the deformation of IF steel samples subjected to uniform uniaxial tensile strain $\varepsilon_z^a$: (a) gradient sample consisting of two grain size gradient surface layers (GSL) sandwiching a coarse-grained (CG) core, in which $h_t$ is the half thickness of the whole sample; (b) homogeneous sample. Note the non-uniform deformation on the lateral surface of the gradient sample in (a).

the properties of these individual layers through volume averaging. The results and discussion will be given in Section 3, which is followed by conclusions (Section 4).

## 2. Constitutive model for gradient structure

A gradient IF steel sample is assumed to be a perfectly-bonded multilayered structure. The grain size is assumed to be uniformly distributed in each layer (called homogeneous layer). The constitutive behavior of the constituent homogeneous layers with different grain size will be established first by using two sub-models, i.e., the nanocrystalline (NC) sub-model for layers with grain size varying from tens of nanometers to several hundred nanometers (called NC layers), while the micro-crystalline (MC) sub-model is for those with grain size ranging from submicrometer to tens of micrometers (called MC layers). We assume that there are $n$ layers in the gradient region, and the CG core can be viewed as the $(n+1)$-th layer, where the sample is subjected to uniaxial tension in $z$ direction (Figs. 2a and 3a). The lateral and thickness directions are set as $x$ and $h$ (or $y$), respectively. Therefore, the $z$-$h$ plane is the lateral surface (Fig. 2a).

In order to describe how the surface non-uniform deformation forms, we first consider the deformation of free-standing layers with different grain sizes ($i = 1, 2, ..., n+1$, and grain size increases as $i$ increases) subjected to uniaxial tensile strain $\varepsilon_z^a$, as shown in Fig. 3a. Generally, the free-standing layers with smaller grain sizes (outer layers) are more prone to plastic instability (or necking/shrinking in the lateral ($x$) direction) than those with larger grain sizes (inner layers). Hence, the shrinking magnitude in the necked region, i.e., $-\varepsilon_{xi}w$, or $\varepsilon_{zi}w/2$ for incompressible material, varies in different layers (Fig. 3b). The subscripts $x$ and $z$ denote directions and $i$ represents the $i$-th layer. In the gradient structure, the interaction between different layers will modify the deformation behavior of each layer, that is, the faster lateral necking of the outer layers is suppressed by the higher capability of the inner layers to resist plastic instability, which produces the surface non-uniform deformation, as schematically shown by the curved boundary in Fig. 3c. According to Ashby (Ashby, 1970), the non-uniform deformation is able to inject GNDs into the gradient sample (Fig. 3c). We assume that all GNDs in the gradient sample are induced by the surface non-uniform deformation. As a result, the effect of layer interfaces can be considered by incorporating GNDs in the present constitutive model. In the following, we will first provide the constitutive framework for gradient
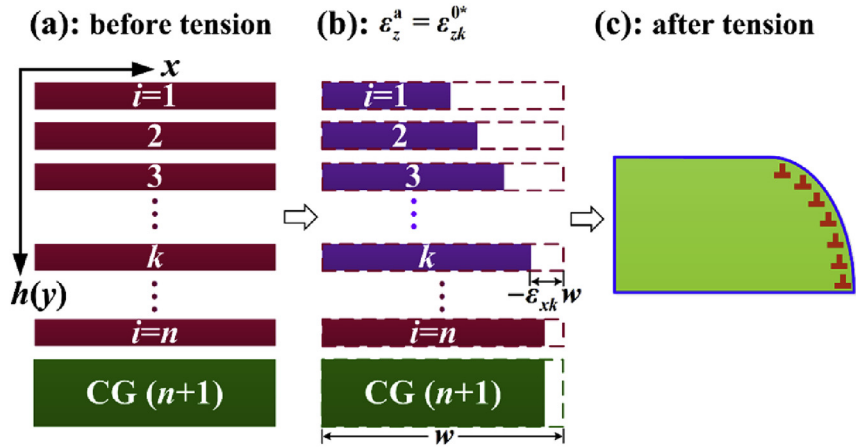
**Fig. 3.** The formation of non-uniform deformation on the lateral surface (z-h plane) of a gradient sample. (a) free-standing layers with different grain sizes before tension; (b) free-standing layers during deformation as layer k starts necking in the lateral (x) direction; (c) gradient structure with injections of GNDs after tension.

structure based on the conventional strain gradient theory of plasticity (Huang et al., 2004) and Kocks-Mecking-Estrin (KME) model (Estrin and Mecking, 1984) with flow stress modified (Section 2.1). The surface non-uniform deformation and the GNDs density are then calculated by obtaining the shrinking strain of each layer ($\varepsilon_{xi}$ or $\varepsilon_{zi}$) using a Marciniak-Kuczyński (M-K) type analysis (Marciniak et al., 1973) and by transforming the gradient problem into a plane strain thermal stress one for the sake of easy solution using finite element simulations (Section 2.2).

The total strain rate tensor $\dot{\varepsilon}$ for each constituent layer can be expressed as (the layer index $i$ is omitted for clarity):

$$\dot{\boldsymbol{\varepsilon}} = \frac{1}{2\mu}\dot{\boldsymbol{\sigma}}' + \frac{1-2\nu}{3E}\boldsymbol{\delta\delta}:\dot{\boldsymbol{\sigma}} + \frac{3\dot{\varepsilon}^{\mathrm{p}}}{2\sigma}\boldsymbol{\sigma}', \tag{1}$$

where $\boldsymbol{\sigma}$ is the stress tensor and a dot denotes differentiation with respect to time $t$; and $\boldsymbol{\delta}$, $\boldsymbol{\sigma}'=\boldsymbol{\sigma}-\boldsymbol{\delta\delta}{:}\boldsymbol{\sigma}/3$, $\sigma=\sqrt{3\boldsymbol{\sigma}':\boldsymbol{\sigma}'/2}$, $\dot{\varepsilon}^{\mathrm{p}}$, $\dot{\varepsilon}^{\mathrm{p}} = \sqrt{2\dot{\boldsymbol{\varepsilon}}^{\mathrm{p}}:\dot{\boldsymbol{\varepsilon}}^{\mathrm{p}}/3}$, $E$, $\mu$ and $\nu$ are Kronecker's delta, deviatoric stress, equivalent von Mises stress, plastic strain rate, equivalent von Mises plastic strain rate, Young's modulus, shear modulus and Poisson's ratio, respectively. A kinetic equation is then applied to correlate $\dot{\varepsilon}^{\mathrm{p}}$ and $\sigma$ as (Huang et al., 2004):

$$\dot{\varepsilon}^{\mathrm{p}} = \dot{\varepsilon}\left(\sigma\big/\sigma_{\mathrm{f}}\right)^m, \tag{2}$$

where $\dot{\varepsilon} = \sqrt{2\dot{\boldsymbol{\varepsilon}}':\dot{\boldsymbol{\varepsilon}}'/3}$ ($\dot{\boldsymbol{\varepsilon}}' = \dot{\boldsymbol{\varepsilon}} - \boldsymbol{\delta\delta}:\dot{\boldsymbol{\varepsilon}}/3$ is the deviatoric strain rate), $\sigma_{\mathrm{f}}$ and $m$ are the equivalent strain rate, flow stress and rate-sensitivity exponent, respectively. The flow stress $\sigma_{\mathrm{f}}$ for the component homogeneous NC and MC layers in gradient structure will be addressed in the following subsection 2.1.

Specifically, for incompressible material ($v = 0.5$) as adopted in the present analysis, the constitutive equations of each layer (Eq. (1)) in the gradient structure subjected to uniform uniaxial tension $\dot{\varepsilon}_z^a$ can be specified as (i.e., Eq. (A.5) in Appendix A), see Fig. 2a for the coordinate system used:

$$\dot{\varepsilon}_x = \frac{1}{2}\left(\frac{1}{2\mu}\dot{\sigma}_x + \eta\sigma_x\right) - \frac{1}{2}\dot{\varepsilon}_z$$

$$\dot{\varepsilon}_y = -\frac{1}{2}\left(\frac{1}{2\mu}\dot{\sigma}_x + \eta\sigma_x\right) - \frac{1}{2}\dot{\varepsilon}_z, \tag{3}$$

$$\dot{\gamma}_{xy} = \frac{1}{\mu}\dot{\tau}_{xy} + 2\eta\tau_{xy}$$

where $\eta = \frac{3\dot{\varepsilon}^{\mathrm{p}}}{2\sigma}$. Here, considering the geometry of each layer with thickness much less than the other two dimensions, we adopted the assumption of $\sigma_y=0$, as used in the optimal, shear-lag model for multi-layered elastic structure (Nairn and Mendels, 2001). The above assumption has been validated by the following finite element calculations (Appendix D and Supplementary Note 1), which shows that the magnitude of $\sigma_y$ is ignorable as compared with those of $\sigma_x$ and $\sigma_z$ except in only a very small region near the right (lateral) surface (Supplementary Fig. 1b). Eqs. (2)–(3) describe the triaxial constitutive relations for all component layers of different grain sizes in a gradient structure subjected to uniaxial tension.

## 2.1. Flow stress for component homogeneous layers

The flow stress in the NC layers can be approximated as:

$$\sigma_f = \sigma_0 + M\alpha\mu b\sqrt{\rho_s + \rho_G} + \sigma_b + \sigma_{GB}, \tag{4}$$

where $M$, $\alpha$, $b$, $\rho_s$, $\rho_G$, $\sigma_b$ and $\sigma_0$ are the Taylor factor, Taylor constant, magnitude of the Burgers vector, statistically stored dislocation density, GNDs density, back stress and lattice friction stress, respectively. The GNDs density in gradient structure has been given by Li et al. (2015a). The essential expressions are summarized here for completeness. All GNDs are assumed to be edge type and positioned uniformly along the lateral ($x$) direction (Fig. 3c). The dislocation line of each GND is idealized as a straight line running through the entire sample along the tensile ($z$) direction (Figs. 2a and 3c). Therefore, the total length of the GNDs $\zeta$ injected by the non-uniform lateral deformation in the unit layer with thickness $\Delta h$ can be expressed as

$$\zeta = \frac{l\Delta h}{s} = \frac{la}{b}, \tag{5}$$

where $l$ is the total length of the gradient sample (Fig. 2a), $s=b(\Delta h/a)$ is the spacing between individual slip steps near the lateral surface, $a$ (>0) is the displacement difference along the $x$-axis between two adjacent deformed layers, which characterizes the lateral surface non-uniform deformation. By assuming that all GNDs are uniformly distributed in each layer, the volume occupied by GNDs can be approximated as $V = l(\Delta h)^2$. Thus, the GNDs density can be given as

$$\rho_G = \frac{\zeta}{V} = \frac{a}{b(\Delta h)^2}. \tag{6}$$

On the other hand, the predicted GNDs density (Eq. (6)) can be evaluated by the measured hardness along the sample depth since it is difficult to measure GNDs density directly. By using Tabor's factor $\lambda$ to convert the flow stress $\sigma_f$ (Eq. (4)) to the measured hardness, i.e., $H = \lambda\sigma_f = \lambda(\sigma_0 + \sigma_{GB} + \sigma_b + M\alpha\mu b\sqrt{\rho_s + \rho_G})$, we have

$$H - H_0 = \lambda M\alpha\mu b\sqrt{\rho_s + \rho_G}, \tag{7}$$

where $H_0 = \lambda(\sigma_0 + \sigma_{GB} + \sigma_b)$ represents the hardness along the thickness on the lateral surface of gradient sample before deformation. As for free standing component layers after deformation without incorporating GNDs (i.e., $\rho_G = 0$), their hardness $H_s$ can be obtained from Eq. (7), i.e.,

$$H_s - H_0 = \lambda M\alpha\mu b\sqrt{\rho_s}. \tag{8}$$

By combining Eqs. (7) and (8), $\rho_G$ can be expressed as

$$\rho_G = \frac{(H - H_0)^2 - (H_s - H_0)^2}{(\lambda M\alpha\mu b)^2}. \tag{9}$$

The hardness parameters $H$, $H_0$ and $H_s$ can be measured through experiments (Fig. 2c of Wu et al., 2014a).

As observed in experiments (Yang et al., 2016), back stress plays a role in enhancing strain hardening of gradient structure. The back stress in the gradient structure is a long range internal stress caused by the interaction and pile-up of GNDs near the layer interfaces. Since it is the spatial variation of GNDs density that contributes to the long-range internal stress (Bayley et al., 2006; Evers et al., 2004; Groma et al., 2003; Yefimov et al., 2004), the internal stress resulted from single edge GND can be given as (Bayley et al., 2006)

$$\sigma_x = \frac{3\mu bR^2}{8(1-\nu)}\frac{\partial\rho_G}{\partial y}, \sigma_{xy} = -\frac{\mu bR^2}{8(1-\nu)}\frac{\partial\rho_G}{\partial x}$$

$$\sigma_y = \frac{\mu bR^2}{8(1-\nu)}\frac{\partial\rho_G}{\partial y}, \sigma_{xz} = 0, \tag{10}$$

$$\sigma_z = \frac{\mu b\nu R^2}{2(1-\nu)}\frac{\partial\rho_G}{\partial y}, \sigma_{yz} = 0$$

where $R$ is the integral circular domain for GNDs to contribute to the back stress. Based on the assumption that GNDs are positioned uniformly along the $x$ direction in each unit layer, we have $\frac{\partial\rho_G}{\partial x} = 0$, and $\frac{\partial\rho_G}{\partial y}$ can be approximated as $\frac{\Delta\rho_G}{\Delta h}$, in which $\Delta\rho_G$ is the difference of GNDs density between neighboring layers. Then the non-zero internal stress components are $\sigma_x$, $\sigma_y$ and $\sigma_z$. As a result, the GNDs-induced back stress can be approximated as the von-Mises equivalence of the above stress components, i.e.,

$$\sigma_b = \sqrt{16v^2 - 16v + 7} \, \frac{\mu b R^2}{8(1-v)} \frac{\Delta \rho_G}{\Delta h}. \tag{11}$$

The parameter $R$ should be in the order of layer thickness $\Delta h$ in order to model the interaction of adjacent layers. The last term $\sigma_{GB} = k_{HP}/d$ in flow stress arises from a Hall-Petch type strengthening due to the refined grains (Capolungo et al., 2007; Carvalho Resende et al., 2013; Delince et al., 2007), where $k_{HP}$ is a constant Hall-Petch slope, and $d$ denotes grain size.

The evolution of statistically stored dislocation density $\rho$ with respect to plastic strain can be expressed as:

$$\frac{d\rho_s}{d\varepsilon^p} = M(k + k_1 \sqrt{\rho_s} - k_2 \rho_s - k_e \rho_s), \tag{12}$$

where $k = k_3/(bd)$, $k_1 = \psi/b$, $k_2 = k_{20}(\dot{\varepsilon}^p/\dot{\varepsilon}_0)^{-1/n_0}$, $\psi$ is a proportionality factor, $k_{20}$ and $\dot{\varepsilon}_0$ are material constants, $k_3$ is a geometric factor related to the grain shape and proportion of dislocations arriving at the grain boundaries, $n_0$ is inversely proportional to temperature (Estrin and Mecking, 1984), and $k_e = (d_e/d)^2$ is an additional dynamic recovery factor, where $d_e$ is a reference grain size corresponding to the critical grain size at which enhanced dynamic recovery occurs (Li and Soh, 2012b).

The expressions of the flow stress for MC layers are set to be the same as those of NC layers, but with different values for parameters according to experimental observations (Wu et al., 2014a), such as Hall-Petch slope $k_{HP}$, reference grain size $d_e$ and dynamics recovery factor $k_2$. This makes the two sub-models consistent.

## 2.2. Calculation of GNDs density and back stress

The objective of this section is to calculate the GNDs density presented in Eq. (6) and back stress in Eq. (11) by solving the 3-D plastic deformation problem of a gradient structure subjected to uniaxial tension, i.e., Eqs. (2) and (3). As for the layers without considering GNDs (i.e., $\rho_G = 0$, $\sigma_b = 0$), these equations can be solved numerically independently layer by layer. However, for the layers with GNDs injected by the lateral surface non-uniform deformation, the above equations should be solved by combining all the component layers. The key is to calculate the magnitude of shrinking of each layer (Fig. 3b), that is, $\varepsilon_{zi} (= -2\varepsilon_{xi})$ as appeared in Eq. (3). Fig. 3b shows that as the applied strain of the gradient structure approaches the limit strain of the $k$-th layer, i.e., $\varepsilon_z^a = \varepsilon_{zk}^{0*}$ (the strain in the section of uniform deformation as a neck sets in), it starts shrinking/necking. The strain in the necked region along $z$ direction, i.e., $\varepsilon_z$, for layer $k$ is $\varepsilon_{zk} = -2\varepsilon_{xk} = \varepsilon_{zk}^* = \chi_k \varepsilon_{zk}^{0*} = \chi_k \varepsilon_z^a$, where $\varepsilon_{zk}^*$ is the critical strain in the necked region and $\chi_k = \varepsilon_{zk}^*/\varepsilon_{zk}^{0*}$ is the limit strain ratio. The values of $\varepsilon_{zk}^{0*}$ and $\varepsilon_{zk}^*$ can be calculated using the following M-K analysis. Moreover, the layers 1-($k$-1) have already necked since their limit strains are smaller than that of the layer $k$. However, in order to model the surface non-uniform deformation, we assume that they are able to afford to deform even after necking. This assumption is conceivable because in a gradient structure the necking of the layers 1-($k$-1) could be suppressed by the inner layers with better resistance to plastic instability, as schematically shown in Fig. 3b. The $\varepsilon_z$ of these layers are set to be similar in form to that of the $k$-th layer, i.e., $\varepsilon_{zi} = \chi_i \varepsilon_z^a$, $i = 1, 2, \ldots, (k-1)$, where $\chi_i$ has the same definition as the above $\chi_k$. Finally the $\varepsilon_z$ in the stable layers ($i = (k+1), (k+2), \ldots, (n+1)$) are identical to the applied strain $\varepsilon_z^a$, i.e., $\varepsilon_{zi} = \varepsilon_z^a$. As a result, the $z$-component strains for all component layers in a gradient structure subjected to uniaxial tensile strain $\varepsilon_z^a$ ($\varepsilon_z^a = \varepsilon_{zk}^{0*}$) can be summarized as

$$\varepsilon_{zi} = \begin{cases} \chi_i \varepsilon_z^a, & \text{if } \varepsilon_z^a \geq \varepsilon_{zi}^{0*} \quad \text{(for necked layers,} \quad i = 1, 2 \ldots, k) \\ \varepsilon_z^a, & \text{if } \varepsilon_z^a < \varepsilon_{zi}^{0*} \quad \text{(for stable layers,} \quad i = k+1, k+2, \ldots, n+1) \end{cases} \tag{13}$$

The values of $\chi_i$ for the $i$-th layer will be obtained by implementing M-K analysis based on the constitutive behavior of layer $i$ without incorporating GNDs (i.e., $\rho_G = 0$).

The original M-K method is aimed at analyzing sheet necking behavior and calculating the forming limit diagrams of the sheets by introducing an initial non-uniformity (Hutchinson and Neale, 1978; Marciniak et al., 1973). Therefore, M-K analysis is an appropriate approach to find the limit strain ratio $\chi_i$ of layer $i$ as defined above because the free-standing component layers in a gradient sample could be viewed as a sheet. The M-K analysis used here is along the line of that by Hutchinson and Neale (1978) but using the material behavior developed in the present model. For brevity, the subscript '$i$' is omitted whenever there is no danger of confusion. Assume the material is rigid-plastic and incompressible, the law of plastic flow (Eq. (1)) becomes

$$d\boldsymbol{\varepsilon} = \frac{3}{2} \frac{d\varepsilon}{\sigma} \boldsymbol{\sigma}', \tag{14}$$

where $d\varepsilon = 2d\boldsymbol{\varepsilon} : d\boldsymbol{\varepsilon}/3$. The yield condition is $\sigma = \sigma_f$ for rigid-plastic material (see Eq. (2)), and for plane stress condition $\sigma = \sqrt{\sigma_z^2 - \sigma_z \sigma_x + \sigma_x^2}$. The detailed M-K analysis is given in Appendix C, which yields two differential equations for solving the

equivalent strains $\varepsilon^0$ in the uniform section and $\varepsilon$ in the necked region, i.e., Eqs. (C.9) and (C.11). The two equations can be rewritten as

$$
\frac{d\varepsilon^0}{d\varepsilon} = \pm\sqrt{\frac{1}{B} - \frac{1}{(1-\xi)^2}\frac{1-B-G}{B}\left(\frac{\sigma^0}{\sigma}\right)^2 \exp\left(-2C\varepsilon^0 - 2\varepsilon_y\right)},
$$
$$
\frac{d\varepsilon_y}{d\varepsilon} = -\frac{A\sqrt{1-B-G}}{(1-\xi)}\frac{\sigma^0}{\sigma}\exp\left(-C\varepsilon^0 - \varepsilon_y\right) - D\frac{d\varepsilon^0}{d\varepsilon}
\tag{15}
$$

where $\xi$ is the initial geometric non-uniformity, and the expressions of $A$, $B$, $C$, $D$ and $G$ are given in Appendix C. Physically, the value of $d\varepsilon^0/d\varepsilon$ should be selected as positive. Now we can use the fourth-order Runge-Kutta method to solve the two differential equations in (15), which gives the variation of $\varepsilon^0$ with respect to $\varepsilon$, then the critical strain $\varepsilon_z^*$, $\varepsilon_z^{0*}$, and the ratio $\chi = \varepsilon_z^*/\varepsilon_z^{0*}$ as well can be obtained by using the criterion $d\varepsilon^0/d\varepsilon=0$.

After getting the value of $\varepsilon_z$ in Eq. (3) for each layer, it is ready to solve the plastic deformation problem of gradient structure subjected to uniaxial tension. However, since the value of $\eta$ differs in different layers and it evolves during deformation, it is difficult, even not impossible, to solve them numerically. In this study, the above difficulty has been circumvented by transforming the above 3-D plastic deformation problem into a plane strain problem of the same structure subjected to thermal load $\dot{T}$. In the following, we will prove this transformation.

As for a gradient structure in plane strain condition subjected to thermal load $\dot{T}$, the constitutive relations of each layer are given as follows (Appendix B).

$$
\dot{\varepsilon}_x = \frac{1}{2}\left(\frac{1}{2\mu}\dot{\sigma}_x + \eta\sigma_x\right) + \frac{3}{2}\alpha\dot{T}
$$
$$
\dot{\varepsilon}_y = -\frac{1}{2}\left(\frac{1}{2\mu}\dot{\sigma}_x + \eta\sigma_x\right) + \frac{3}{2}\alpha\dot{T}
$$
$$
\dot{\gamma}_{xy} = \frac{1}{\mu}\dot{\tau}_{xy} + 2\eta\tau_{xy}
\tag{16}
$$

where $\alpha$ is thermal expansion coefficient. Compare Eqs. (3) and (16), if we set $\frac{3}{2}\alpha\dot{T} = -\frac{1}{2}\dot{\varepsilon}_z$, and by integration we get $\frac{3}{2}\alpha\Delta T = -\frac{1}{2}\varepsilon_z$. Then by setting $\Delta T=-1°C$, we have

$$
\alpha = \frac{1}{3}\varepsilon_z.
\tag{17}
$$

Now the two sets of equations turn out to be identical. That is, the solution of the 3-D plastic deformation problem of a gradient sample subjected to uniaxial tension, i.e., Eqs. (2) and (3), is equivalent to that of a plane strain thermal-stress problem, i.e., Eqs. (2) and (16). The latter can be easily solved by finite element simulations (Appendix D), which yields the values of the non-uniform deformation parameter $a$, and the GNDs density and back stress, see Eqs. (6) and (11).

### 2.3. Overall mechanical response of gradient structure

Since the focus of the present study is on uniaxial tensioning of gradient structure in which the sample is subjected to uniaxial uniform strain $\varepsilon_z^a$ through its thickness in experiments, the overall stress-strain response $\sigma_z^G$ in the gradient sample can be approximately obtained through volume averaging over all the component layers as:

$$
\sigma_z^G = \frac{\sum_{i=1}^{n^*}\sigma_{zi}^{GND}h_i}{h_t},
\tag{18}
$$

where $\sigma_{zi}^{GND}$ denotes the z-component stress of layer $i$ in the gradient sample considering both GNDs and back stress; $h_i$ and $h_t$ are the thickness of layer $i$ and that the half thickness of the entire gradient sample, respectively; and $n^*$ is the layer number of the whole sample adopted in the finite element model. According to the experimental measurements (Wu et al., 2014a), the grain size $d$ along the sample thickness $h$ in the gradient region can be approximated as $log_{10}(d)=a_gh^2+b_g$, where $a_g$ and $b_g$ are constants depending on the grain size of the topmost phase $d_1$ and CG core $d_c$. In order to calculate the uniform elongation of the homogeneous or gradient IF steel samples, Considère criterion is implemented, i.e., $d\sigma_z^G/d\varepsilon_z^a \leq \sigma_z^G$. As for yield strength, it is commonly defined as 0.2% offset stress.

## 3. Results and discussion

Since the MC model is proposed for homogeneous IF steels with grain size ranging from submicrometer to tens of micrometers, while the NC model is for those with grain size varying from tens of nanometers to submicrometer, and considering that (i) the existing modified versions of KME models for coarse- and fine-grained metals can be applied down to 1 μm (Delince et al., 2007) and those for nano- and ultrafine-grained metals can be applied up to 583 nm (Liu and Mishnaevsky Jr., 2014); and (ii) the enhanced dynamic recovery usually occurs in submicrometers, e.g., 700 nm for copper (Duhamel et al., 2010), the boundary should lie in the range of submicrometers. The boundary value is determined to be 680 nm by fitting the model predictions with the experimental data so that the proposed model could be able to describe accurately the grain size dependence of the constitutive behavior of homogeneous IF steels with grain sizes ranging from nanoscale to microscale (Figs. 4 and 5). The main difference between the two sub-models lies in the specific values of the parameters in Hall-Petch constants $\sigma_0$ and $k_{HP}$ as well as the dynamic recovery factors $k_2$ and $k_e$ (or $d_e$) due to the grain size effect. The Hall-Petch constants should be set as different for the two sub-models according to the experimental measurements that the Hall-Petch slope ($k_{HP}$) in the submicrometer to micrometer range is smaller than that in the nanometer to submicrometer range, whereas the corresponding lattice frictional stress ($\sigma_0$) is larger for the former than the latter (Fig. 5a). The dynamic recovery factor $k_2$ of NC sub-model should be larger than that of MC sub-model because the dynamic recovery is much larger in refined grains than that in larger grains due to the sharply increased grain boundary region volume fraction as grain size is reduced down into nanoscale (Meyers et al., 2006). For the same reason, the reference grain size $d_e$ in $k_e = (d_e/d)^2$ corresponding to the initiation of enhanced dynamic recovery should also be smaller in NC model than that in the MC model. There are totally seven adjustable parameters in the proposed model; and all can be determined by fitting with experimental data while the material and geometric parameters are directly taken from experiments or existing KME models. The number of the layers in the gradient region, i.e., $n_g$, has been selected to be large enough to enable each layer to have homogeneous grain structure, as demonstrated in Supplementary Note 2. The Tabor's factor is determined by dividing the measured
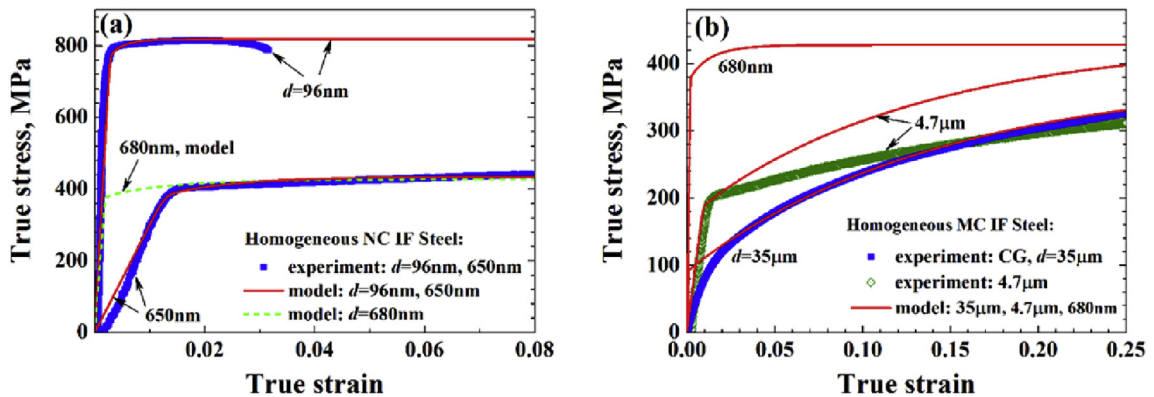


**Fig. 4.** True stress-true strain relations of homogeneous IF steel samples predicted by the proposed NC (a) and MC (b) sub-models. The experimental data for $d$ = 96 nm, 650 nm, 4.7 μm and CG IF steel samples are included for comparison.
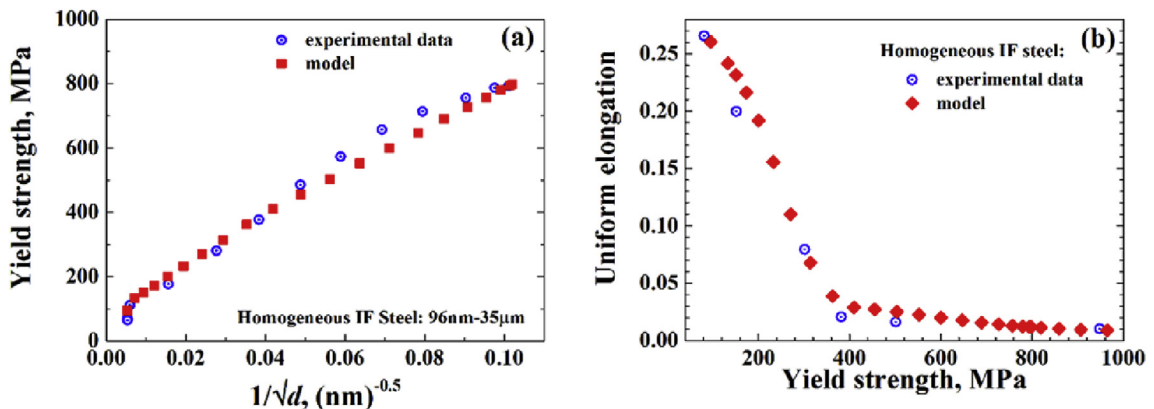


**Fig. 5.** The predicted Hall-Petch relation (a) and strength-ductility relation (b) for homogeneous IF steel samples with grain sizes ranging from tens of nanometers to tens of micrometers. The experimental data for the two relations are also included for comparison.

**Table 1**
Material parameters for NC and MC IF steel samples.

| Parameter | Symbol | NC IF steel | MC IF steel |
|---|---|---|---|
| Grain size | $d$ | 10 nm–680 nm | 680 nm–35 μm |
| Elastic modulus (GPa) | $E$ | 200 | 200 |
| Shear modulus (GPa) | $\mu$ | 77 | 77 |
| Poisson's ratio | $\nu$ | 0.28 | 0.28 |
| Magnitude of Burgers vector (nm) | $b$ | 0.26 | 0.26 |
| Taylor factor | $M$ | 3.06 | 3.06 |
| Taylor constant | $\alpha$ | 0.3 | 0.3 |
| Hall-Petch slope (MPa·m$^{1/2}$) | $k_{HP}$ | 0.194 | 0.252 |
| Lattice frictional stress (MPa) | $\sigma_0$ | 110.3 | 40 |
| Tabor's factor | $\lambda$ | 3.23 | 3.23 |
| Rate sensitivity exponent | $m$ | 20 | 20 |
| Proportionality factor | $\psi$ | 0.019 | 0.019 |
| Dynamic recovery factor | $k_2$ | 29.05 | 4.5 |
| Dynamic recovery constant 1 | $k_{20}$ | 21 | 3.25 |
| Dynamic recovery constant 2 | $n_0$ | 21.25 | 21.25 |
| Geometric factor | $k_3$ | 0.05 | 0.05 |
| Reference strain rate (s$^{-1}$) | $\dot{\varepsilon}_0$ | 1 | 1 |
| Applied total strain rate (s$^{-1}$) | $\dot{\varepsilon}_z^a$ | $1\times10^{-3}$ | $1\times10^{-3}$ |
| Reference grain size | $d_e$ | 950 nm | 3.5 μm |
| Initial dislocation density (m$^{-2}$) | $\rho_0$ | $3 \times 10^{12}$ | $3 \times 10^{12}$ ($2 \times 10^{11}$ for CG) |
| Original orientation of the groove | $\beta$ | 25.3° | 25.3° |
| Initial geometric non-uniformity | $\xi$ | 0.015 | 0.015 |
| Proportional loading ratio (uniaxial tension) | $r$ | −0.5 | −0.5 |

hardness of the topmost layer (with grain size of 96 nm) of the gradient IF steel sample with $h_g = 120$ μm by its yield strength. The parameter values used in the analysis are listed in Tables 1 and 2. In addition, except otherwise stated, the experimental data used in the present analysis for comparison with the model predictions have all been adopted from the experiments of Wu et al. (2014a). For brevity no more statement on them will be given further.

### 3.1. Stress-strain curves of homogeneous IF steels

The constitutive behavior of homogeneous NC and MC IF steel samples without incorporating GNDs ($\rho_G=0$) and back stress ($\sigma_b=0$) predicted by the proposed model will be validated first before investigating the overall mechanical response of gradient structure. Fig. 4 presents the predicted true stress-true strain curves for several NC and MC IF steel samples with grain size $d = 35$μm, 4.7 μm, 680 nm, 650 nm and 96 nm; and the corresponding experimental data for $d = 35$μm, 4.7 μm, 650 nm and 96 nm are included for comparison. The elastic moduli of the predicted curves are tuned to coincide with the experimental measurements. The two 680 nm curves in (a) and (b) are almost identical but they are respectively predicted by the NC and MC sub-models. It can be clearly shown that the predicted curves are in good agreement with the experimental data in terms of both strength and strain hardening behavior except the case of $d = 4.7$ μm. In the latter case the yield strength and uniform elongation measured in experiments (i.e., 188.7 MPa and 21.7%) are also well reproduced by the proposed model (i.e., 192.85 MPa and 21.5%) in spite of predicting higher flow stress. The lower measured flow stress is might due to the specific situation of the tested sample such as annealing technique and microstructure. In order to obtain an overview of the predictive capability of the proposed model for homogeneous IF steel samples, we also plotted the Hall-Petch relation and the yield strength-uniform elongation map predicted by the model, as presented in Fig. 5a and b, respectively. The overall quantitative agreement between the model prediction and the experimental data demonstrated the validity of the proposed model to identify the constitutive behavior of homogeneous NC and MC IF steels with different grain sizes ranging from nanoscale to microscale. The above results also show that the proposed sub-models could be applied up to a strain of the uniform elongation of the CG sample, i.e., 26% (Fig. 5b).

### 3.2. Lateral surface non-uniform deformation in gradient IF steels

The lateral surface non-uniform deformation can be represented by the height profile that can be obtained from the difference between the lateral ($x$) displacements along the sample depth and that of the topmost layer on the lateral surface. Fig. 6 presents the variation of the calculated height profile with respect to the sample depth $h$ for a gradient IF steel sample ($d_1$=96nm, $d_c$=35μm, $h_g$=120μm, $h_t$=500μm) subjected to various uniaxial tensile engineering strains, i.e., $\varepsilon_z^e = 0.05$, 0.1 and 0.25. Six measured data for height profile at $\varepsilon_z^e = 0.25$ are also included, see the symbols in Fig. 6a. The comparison shows that the predicted height profile agrees quantitatively very well with the experimental data for the case of 0.25, which validates the proposed model's capability to predict the non-uniform deformation on the lateral surface of a gradient structure. With height profile known, the predicted GNDs density can be calculated using Eq. (6), as shown in Fig. 6b. The results show that $\rho_G$

**Table 2**
Material and geometric parameters for gradient IF steel.

| Parameter | Symbol | Magnitude |
|---|---|---|
| Grain size of coarse grained core (μm) | $d_c$ | 35 |
| Grain size of topmost phase (nm) | $d_1$ | 200, 96, 30 or 10 |
| Phase number in the gradient region | $n$ | 20, 24, 49, 50, or 98 |
| Thickness of gradient surface layer (μm) | $h_g$ | 50, 120, 150, 200, 250, 300, 350, 400, or 490 |
| Half thickness of the total sample (μm) | $h_t$ | 500 |
| Half width of the total sample (mm) | $w$ | 1.25 |
| Layer thickness in finite element simulations (μm) | $\Delta h$ | 9 |
| Integral domain for back stress (μm) | $R$ | 3 |

first increases and then decreases with respect to the sample depth, which generates a maximum near the interface between the gradient region and the CG core and that the maximum move towards to the CG core as the applied engineering strain increases from 0.05 to 0.25, i.e., the maximum $\rho_G$ increases from 1.66 to $5.94 \times 10^{13} \mathrm{m}^{-2}$, while the corresponding critical $h$ increases from 53.64 μm to 80.42 μm, see the black balls in Fig. 6b. Fig. 6 also pointed out that the magnitudes of the height profile and the GNDs density are increased considerably as the applied strain rises, which leads to more GNDs and stronger strain hardening in the gradient structure. The GNDs density distributions that are derived from the measured hardness along the sample depth of the gradient sample are also shown in Fig. 6b for comparison (Eq. (9)). Note that it is difficult, even not impossible, to measure the value of hardness of each free standing component layer after deformation, i.e., $H_s$, in the gradient surface layer ($h \in [0, \quad 120 \mu m]$). Here they are approximated as those of the hardness along the sample depth of the free-standing gradient surface layer with thickness of 120 μm. However, all the values of the hardness parameters in Eq. (9) in the CG core ($h \geq 120 \mu m$) has been given in Fig. 2c of Wu et al. (2014a). The comparison for the CG region shows that, although there are some quantitative discrepancies between the predictions and the experimental data, they agree well with each other overall for all the three applied strains. And it is important to note that no parameter adjustment has been made. As for the experimental derivation of GNDs density in the gradient region, there exist also maximums near the interface between the gradient layer and the CG core for all the three applied strains, i.e., the maximum ($\rho_G$, $h$) increases from (98.2 μm, $5.41 \times 10^{13} \mathrm{m}^{-2}$) to (107.23 μm, $11.57 \times 10^{13} \mathrm{m}^{-2}$). The comparison in the gradient layer show that the model predictions are in qualitatively agreement with the experimental data. The quantitative difference might result from the underestimated $H_s$ in Eq. (9) in the gradient layer for the experimental calculations.

### 3.3. Strain hardening in gradient IF steels

The overall true stress-true strain curves of gradient IF steels ($d_1$=96nm, $d_c$=35μm, $h_g$=120μm, $h_t$=500μm) with both GNDs and back stress incorporated are shown in Fig. 7a. The results for the sample with GNDs only and those without GNDs and back stress are also included for comparison. Their corresponding strain hardening rates are presented in Fig. 7b, while Fig. 7c compares the predicted strain hardening rates with the experimental measurements for both CG and gradient samples. Two phenomena are found intriguing. First, there is an upturn appearing in the plot of the strain hardening rate of the gradient sample with GNDs at the strain of around 1.3% (green solid line in Fig. 7b), and the incorporation of back stress
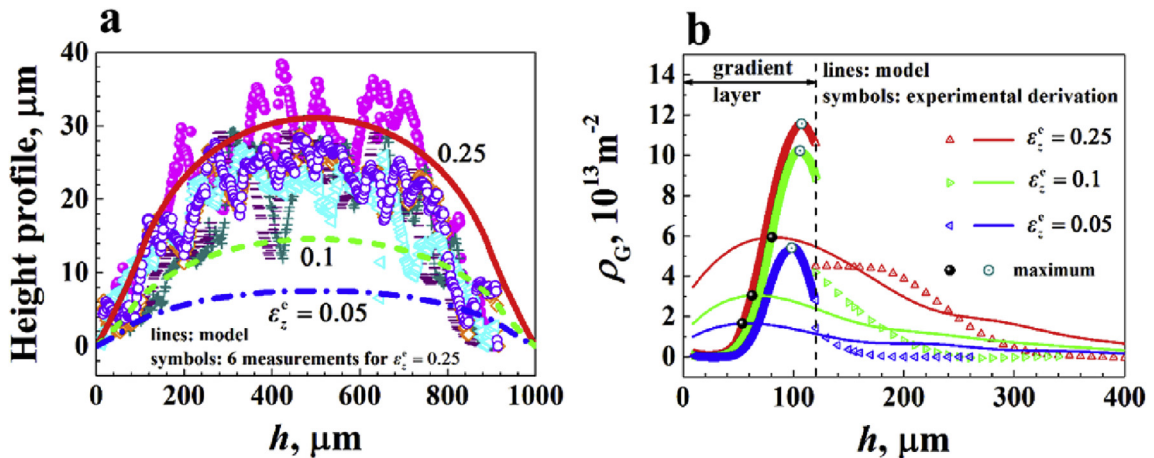


**Fig. 6.** (a) The predicted height profile on the lateral surface of a gradient IF steel sample subjected to various uniaxial tensile engineering strains; and (b) corresponding distribution of GNDs density along the sample depth $h$ (Eq. (6)). The GNDs densities derived from the measured hardness along the sample depth using Eq. (9) are included in (b) for comparison.

further enhances the magnitude (red dashed line). The predicted appearance of the upturn is in quantitatively good accord with the experimental observation, in which the upturn occurs at the strain of around 1.1% (Fig. 7c). This upturn is resulted from the initiation of the injection of the GNDs into all the component layers as the topmost layer starts to neck that is nevertheless suppressed by the other layers with higher plasticity in the gradient structure during uniaxial tension. Second, the strain hardening rate after upturn is even higher than that in CG IF steel sample. The upturn is followed by a decrease of strain hardening that eventually reaches as high as the value of CG sample, see the red dashed line for gradient sample and the
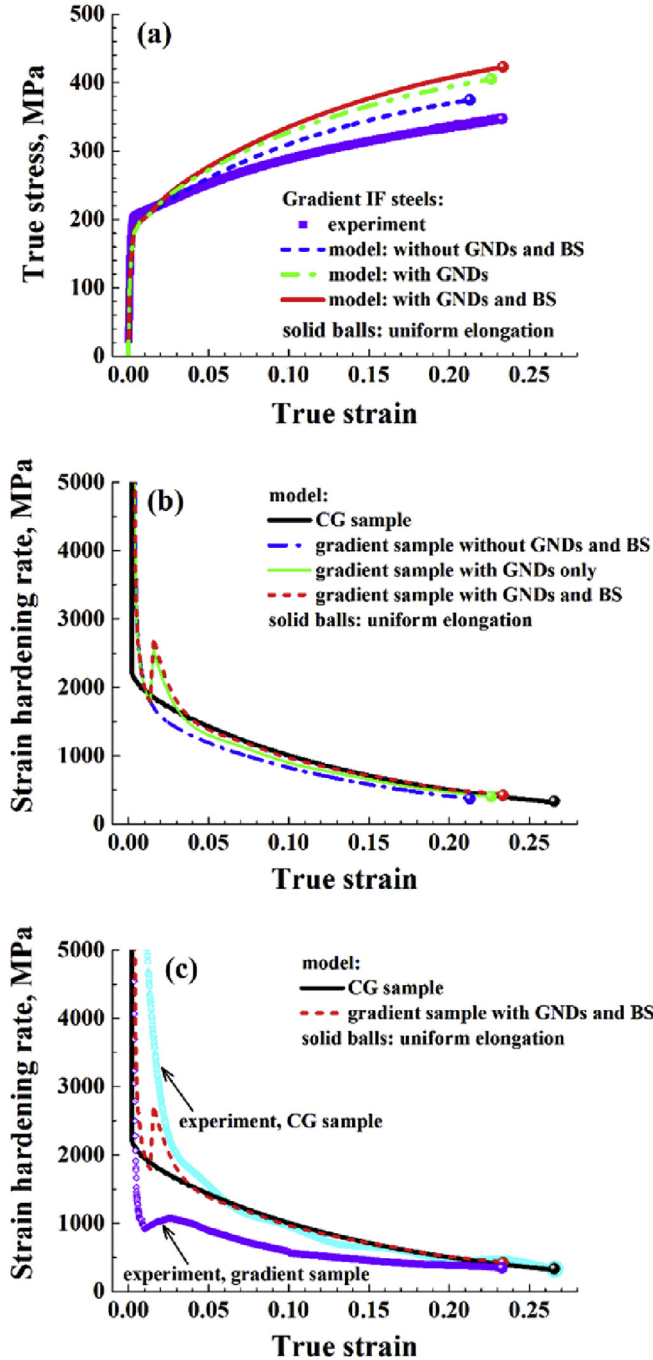


**Fig. 7.** (a) The predicted true stress-true strain curves of gradient IF steel samples incorporating GNDs (and back stress (BS)). The predicted curve of gradient IF steel sample without incorporating GNDs (and BS) and the corresponding experimental data are also included for comparison. (b) The predicted strain hardening rate corresponding to (a). The predicted data for CG sample are also included in (b) for comparison. (c) Comparison of the predictions and the experimental data for both the gradient and CG samples.

black solid line for CG sample. As a result, the upturn enhances considerably the strain hardening capability in the gradient structure, see the red dashed line versus the blue dot-dashed one. Furthermore, Fig. 7c shows that the predicted strain hardening behavior and the experimental observation coincide overall although the predicted value is higher than the measurement for the gradient sample, the reasons of which will be discussed later. Finally the uniform elongation of the gradient IF steel sample with GNDs and back stress is predicted as 0.2336 (red ball in Fig. 7c), which is in good agreement with the experimental value, i.e., 0.2329 (violet ball in Fig. 7c). The predicted yield strength is 177.35 MPa, which is also very close to the experimental datum (205 MPa).

It should be noted from Fig. 7a and c that the predicted flow stress and strain hardening rate after yielding of the gradient IF steel sample are larger than the experimental data. There are possibly three reasons accounting for the over-predictions. The first one could be the assumption of zero $\sigma_y$. The existence of non-zero $\sigma_y$ in the very small region near the lateral surface (Supplementary Fig. 1b) may influence the model predictions. The second one is the simplified assumption of the perfectly bonded multi-layered structure. The idealized layer interface in the present model is actually grain boundary in the real structure. The former is sharp and clear whereas the latter is curved and has many triple junctions. The damage of the actual grain boundary in real gradient structure during deformation could reduce the overall strain hardening capability as compared with the predicted behavior (Fig. 7a and c). The last one might come from the simplified assumption of multi-layered structure with two gradient surface layers and a CG core. Actually, there exists a narrow deformed CG region (around $10-20\mu m$) observed adjacent to the undeformed CG core, in which the grain boundary is not actually high-angle boundary but just sub-grain boundary. However, in the present analysis the deformed CG region with different sub-grain sizes are viewed as different layers with different grain sizes. Therefore, the flow stress of the layers in the deformed CG region is overestimated. That is one of the possible reasons why the predicted flow stress is higher than the experimental data. Considering the complicated gradient microstructure, the predicted curves are in reasonably agreement with the experimental data.
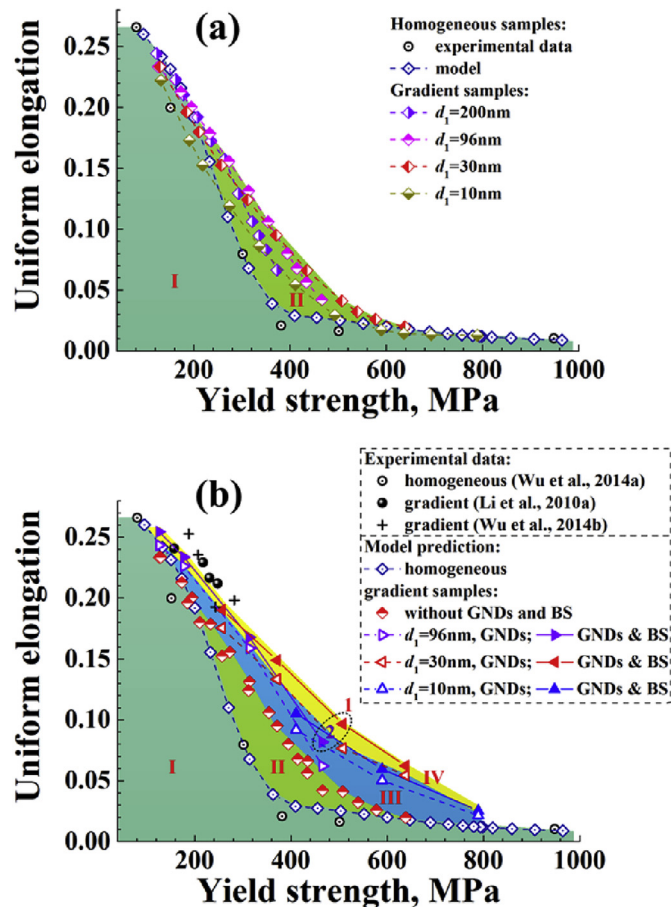


**Fig. 8.** Strength-ductility maps of gradient IF steel samples without (a) (Region II) and with (b) GNDs and back stress (BS) (Regions III and IV). The experimental data for homogeneous (Wu et al., 2014a) and gradient (Li et al., 2010a; Wu et al., 2014b) IF steel samples as well as the model predictions for homogeneous samples are included in (a) and (b) for comparison. In (b), the predicted data without GNDs and back stress for $d_1$=96 and 30 nm as presented in (a) (Region II) and those with GNDs only (Region III) are also included for comparison.

### 3.4. Strength-ductility map for gradient IF steels

In order to comprehensively investigate the effect of GNDs and back stress on the strength-ductility performance, sixteen case studies are conducted to obtain a yield strength-uniform elongation (or strength-ductility) map. The CG core maintains a constant grain size of 35μm, whereas the grain size of the topmost layer $d_1$ is tuned to be 10, 30, 96, and 200 nm. For each $d_1$ the gradient surface layer thickness varies from 50μm to 490μm (with corresponding gradient layer thickness/volume fraction ranging from 10% to 98%) as the half thickness of the total sample keeps constant at 500μm. The strength-ductility map of gradient IF steel without incorporating GNDs and back stress is plotted in Fig. 8a (Region II). The predicted and experimental data for homogeneous IF steel samples are also included for comparison (Region I). The results clearly show that the gradient sample possess better synergy of strength and ductility as compared with the homogeneous samples except small and high strength regions, even though no GNDs are considered.

In addition to the results presented in Fig. 8a, the predicted strength-ductility data of the gradient IF steel samples with GNDs and back stress incorporated (Region IV) are plotted in Fig. 8b. The data of homogeneous samples (Region I), gradient samples without GNDs and back stress (Region II) and gradient samples with GNDs only (Region III) are all included from comparison. The results show that the GNDs and back stress can further considerably enhance the strength-ductility synergy (Regions III and IV) as compared with the gradient samples without them (Region II). Fig. 8b also shows that GNDs play a dominant role (Region III) in enhancing the strength-ductility balance of gradient structure, whereas the back stress plays a minor role (Region IV). The results suggest that in order to gain a good balance of strength-ductility in gradient IF steel sample, the topmost layer grain size should not be too larger or too small and should be less than 100 nm and larger than 10 nm. For example, the $d_1$=30nm, $h_g$=400μm sample possesses a good strength-ductility balance at the strength of 508 MPa and ductility of 9.67%, see the numeral 1 in the oval of Fig. 8b, which are increased by 227 MPa and 7.26% (or 81% and 301% in percent), respectively, as compared with the homogeneous IF steels. By using Considère criterion, a series of experimental strength-ductility data are obtained from the published stress-strain relations for gradient IF steel samples (Li et al., 2010a; Wu et al., 2014b) with $d_c$=35μm, $h_t$=500μm but with different surface mechanical attrition treatment times, which generates different topmost layer grain size $d_1$ and gradient layer thickness $h_g$. The above experimental data are also shown in Fig. 8b for
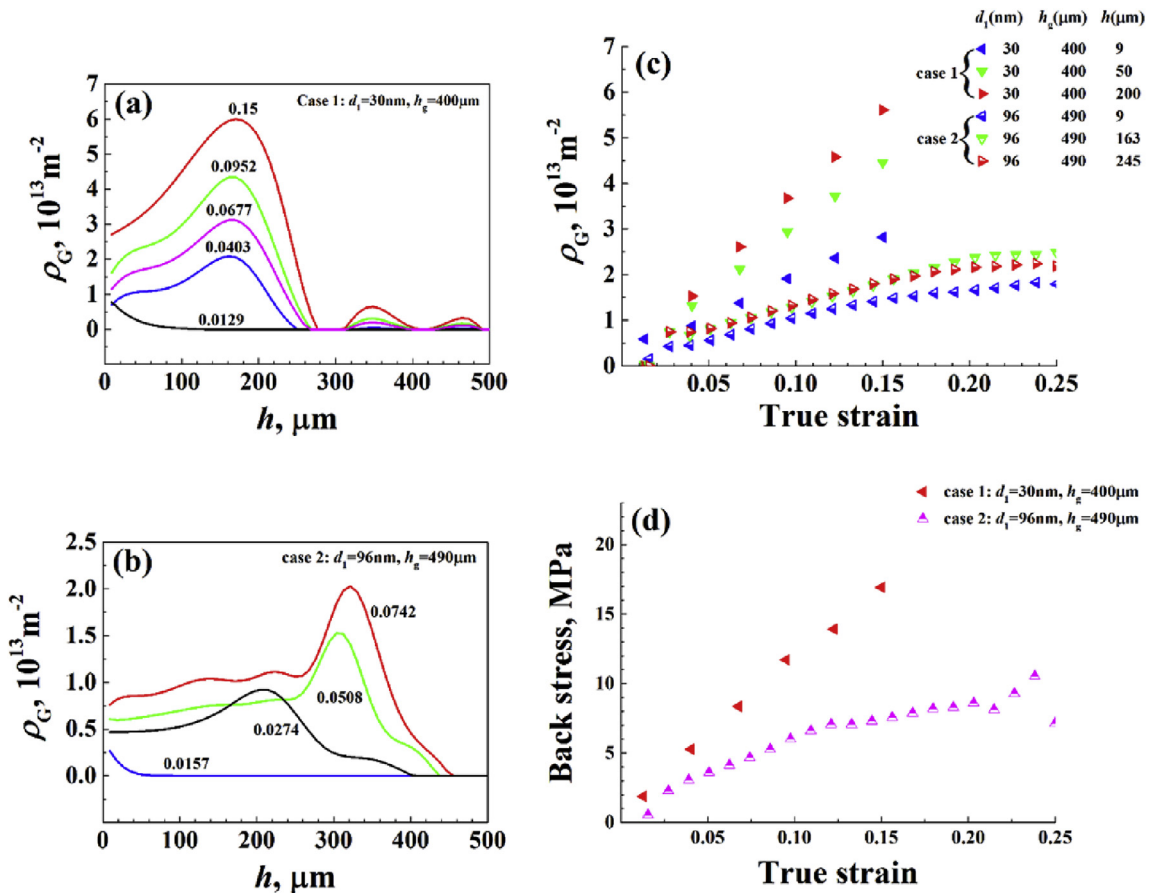


**Fig. 9.** GNDs density distribution in case 1 ($d_1$=30nm, $h_g$=400μm) (a) and case 2 ($d_1$=96nm, $h_g$=490μm) (b) at different applied strains, see the numerals above the lines; and the evolution of GNDs density at different sample depth (c) and back stress (d) with respect to applied strain for the two cases.

comparison. Note that nearly all the experimental data for gradient samples are located along the outer boundary of the yellow region predicted by the proposed model, which clearly demonstrated the proposed model's capability in predicting the strength and ductility of gradient IF steel samples. Fig. 8b also show that the proposed model could be applied up to a strain of at least 25.44% depending on the thickness of the gradient region $h_g$ and the grain size of the topmost layer $d_1$ (Fig. 8b).

Finally, a detailed analysis on GNDs distribution and back stress evolution is made (Fig. 9). Two cases are selected, i.e., $d_1$=30nm, $h_g$=400 μm sample (case 1), and $d_1$= 96 nm, $h_g$=490 μm (case 2) with a strength-ductility synergy of (465.39 MPa, 8.18%) is analyzed (Fig. 9). Note case 1 possesses both higher strength and higher ductility than case 2, see the two symbols in the oval of Fig. 8b. Fig. 9 show that the GNDs density and back stress in case 1 are much higher than case 2. It is noteworthy that the maximum $\rho_G$ of case 1 occurs in small sample depth (161–170 μm) (Fig. 9a), i.e., in nano-grained layers (grain size ranging from 93.9 nm to 106.9 nm for applied strains larger than 0.04), whereas that of case 2 appears in much larger sample depth (205–321 μm) (Fig. 9b), i.e., in micro-grained layers (grain size varying from 0.924 μm to 1.22 μm for applied strains larger than 0.02), which indicates that the nano-grained layers of case 1 has received much more GNDs and thus gained much higher strain hardening capability than case 2. Therefore, the plastic instability of nano-grained layers in case 1 is much more suppressed than case 2. Moreover, the stress-strain relations and the corresponding strain hardening rates for the two cases (Supplementary Fig. 4) show that the strength and enhancements of strain hardening capability thanks to the existence of GNDs and back stress in case 1 are much larger than those in case 2, which undoubtedly leads to a better strength-ductility synergy in the former than the latter.

## 4. Conclusions

In this paper a dislocation density-based theoretical model has been proposed to describe the strain hardening of gradient IF steels by incorporating GNDs that are associated with the non-uniform deformation as experimentally observed on the lateral surface. A principle assumption has been made that all GNDs in the gradient structure are injected by the observed surface non-uniform deformation. The main findings are summarized as follows:

(1) The predicted non-uniform deformation on the lateral surface is in quantitatively good agreement with the measurements for a gradient IF steel sample.
(2) The strain hardening rate up-turn as observed in experiments is well reproduced. The strain hardening rate is able to reach as high as that of coarse-grained sample.
(3) The developed strength-ductility map for gradient IF steel samples show that the strength-ductility performance of gradient samples is remarkably enhanced as compared with their homogeneous counterparts. The predicted map has been verified by a series of experimental data.
(4) By analyzing the GNDs density distribution and back stress evolution in detail, we can conclude that the high strain hardening capability results from the generation of abundant GNDs into the nano-grained layers of the gradient structure.

As a concluding remark, the proposed theoretical framework for gradient nanostructures could be implemented into a finite element scheme as done by (Martínez-Pañeda et al., 2016; Nielsen and Niordson, 2014) to improve the accuracy without imposing some assumptions such as zero stress component along the thickness direction.

## Appendix A. Constitutive equations for a gradient structure subjected to uniaxial tension

As for a gradient structure subjected to uniform uniaxial tension $\dot{\varepsilon}_z$, the constitutive relations (Eq. (1)) for each component layer under incompressible material assumption become

$$\dot{\boldsymbol{\varepsilon}} = \frac{1}{2\mu}\dot{\boldsymbol{\sigma}}' + \eta\boldsymbol{\sigma}', \tag{A.1}$$

The non-zero stresses components are $\sigma_x$, $\sigma_z$ and $\tau_{xy}$, and the non-zero strain components are $\varepsilon_x$, $\varepsilon_y$, $\varepsilon_z$ and $\gamma_{xy}$. By adopting $\sigma_y=0$, the constitutive relations can be specified as

$$
\begin{aligned}
\dot{\varepsilon}_x &= \frac{1}{2\mu}\left(\frac{2}{3}\dot{\sigma}_x - \frac{1}{3}\dot{\sigma}_z\right) + \eta\left(\frac{2}{3}\sigma_x - \frac{1}{3}\sigma_z\right) \\
\dot{\varepsilon}_y &= \frac{1}{2\mu}\left(-\frac{1}{3}\dot{\sigma}_x - \frac{1}{3}\dot{\sigma}_z\right) + \eta\left(-\frac{1}{3}\sigma_x - \frac{1}{3}\sigma_z\right). \\
\dot{\varepsilon}_z &= \frac{1}{2\mu}\left(-\frac{1}{3}\dot{\sigma}_x + \frac{2}{3}\dot{\sigma}_z\right) + \eta\left(-\frac{1}{3}\sigma_x + \frac{2}{3}\sigma_z\right) \\
\dot{\gamma}_{xy} &= \frac{1}{\mu}\dot{\tau}_{xy} + 2\eta\tau_{xy}
\end{aligned}
\tag{A.2}
$$

The incompressible condition is:

$$
\dot{\varepsilon}_x + \dot{\varepsilon}_y + \dot{\varepsilon}_z = 0.
\tag{A.3}
$$

From the first and second equations in (A.2), we have

$$
\dot{\varepsilon}_x - \dot{\varepsilon}_y = \frac{1}{2\mu}\dot{\sigma}_x + \eta\sigma_x.
\tag{A.4}
$$

The combination of Eq. (A.3) and (A.4) yields

$$
\begin{aligned}
\dot{\varepsilon}_x &= \frac{1}{2}\left(\frac{1}{2\mu}\dot{\sigma}_x + \eta\sigma_x\right) - \frac{1}{2}\dot{\varepsilon}_z \\
\dot{\varepsilon}_y &= -\frac{1}{2}\left(\frac{1}{2\mu}\dot{\sigma}_x + \eta\sigma_x\right) - \frac{1}{2}\dot{\varepsilon}_z. \\
\dot{\gamma}_{xy} &= \frac{1}{\mu}\dot{\tau}_{xy} + 2\eta\tau_{xy}
\end{aligned}
\tag{A.5}
$$

## Appendix B. Constitutive relations for a gradient structure subjected to thermal load

As for a gradient structure (in plane strain condition) subjected to thermal load $\dot{T}$, the constitutive relation is

$$
\dot{\varepsilon} = \frac{1}{2\mu}\dot{\sigma}' + \eta\sigma' + \alpha\dot{T}\delta.
\tag{B.1}
$$

Non-zero stress components are $\sigma_x$, $\sigma_z$, $\tau_{xy}$ (the assumption of $\sigma_y=0$ is also adopted here); and non-zero strain components are $\varepsilon_x$, $\varepsilon_y$, and $\gamma_{xy}$. The constitutive relations are given as

$$
\begin{aligned}
\dot{\varepsilon}_x &= \frac{1}{2\mu}\left(\frac{2}{3}\dot{\sigma}_x - \frac{1}{3}\dot{\sigma}_z\right) + \eta\left(\frac{2}{3}\sigma_x - \frac{1}{3}\sigma_z\right) + \alpha\dot{T} \\
\dot{\varepsilon}_y &= \frac{1}{2\mu}\left(-\frac{1}{3}\dot{\sigma}_x - \frac{1}{3}\dot{\sigma}_z\right) + \eta\left(-\frac{1}{3}\sigma_x - \frac{1}{3}\sigma_z\right) + \alpha\dot{T} \\
\dot{\varepsilon}_z &= \frac{1}{2\mu}\left(-\frac{1}{3}\dot{\sigma}_x + \frac{2}{3}\dot{\sigma}_z\right) + \eta\left(-\frac{1}{3}\sigma_x + \frac{2}{3}\sigma_z\right) + \alpha\dot{T} \\
\dot{\gamma}_{xy} &= \frac{1}{\mu}\dot{\tau}_{xy} + 2\eta\tau_{xy}
\end{aligned}
\tag{B.2}
$$

The plane strain condition yields

$$
\dot{\varepsilon}_z = 0.
\tag{B.3}
$$

From (B.3) and the third equation of (B.2), we can derive

$$\frac{1}{2\mu}\left(-\frac{1}{3}\dot{\sigma}_z\right) + \eta\left(-\frac{1}{3}\sigma_z\right) = \frac{1}{2}\left[\frac{1}{2\mu}\left(-\frac{1}{3}\dot{\sigma}_x\right) + \eta\left(-\frac{1}{3}\sigma_x\right) + \alpha\dot{T}\right]. \tag{B.4}$$

Substitute (B.4) into the first and second equations of (B.2), we have

$$\dot{\varepsilon}_x = \frac{1}{2}\left(\frac{1}{2\mu}\dot{\sigma}_x + \eta\sigma_x\right) + \frac{3}{2}\alpha\dot{T}$$

$$\dot{\varepsilon}_y = -\frac{1}{2}\left(\frac{1}{2\mu}\dot{\sigma}_x + \eta\sigma_x\right) + \frac{3}{2}\alpha\dot{T}$$

$$\dot{\gamma}_{xy} = \frac{1}{\mu}\dot{\tau}_{xy} + 2\eta\tau_{xy} \tag{B.5}$$

## Appendix C. M-K type analysis for component layers

Let us consider a free-standing layer with a geometric non-uniformity in the form of a groove or band in the center with an initial thickness $\bar{h}(0)$, while the thickness of the outside region (uniform section) is $\bar{h}_0(0)$, which gives the initial geometric non-uniformity $\xi = [\bar{h}_0(0) - \bar{h}(0)]/\bar{h}_0(0) \geq 0$ (Fig. C.1). Throughout the manuscript, the subscript or superscript '0' denotes the quantities in the uniform section while its absence refer to those in the groove or band. The band width-to-thickness ratio is assumed to be very large. The dashed and solid bands in Fig. C.1 are those before and after deformation, respectively, the orientations of which are $\beta$ and $\gamma$, respectively.
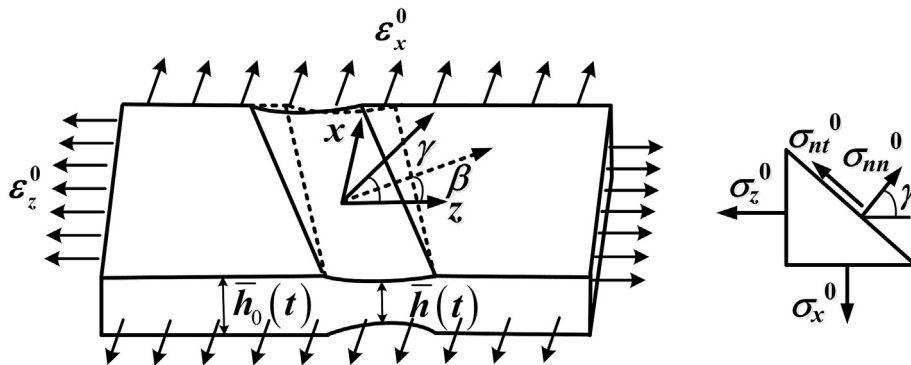


Fig. C.1. Schematic and conventions for M-K analysis for single free-standing layer in a gradient sample. The dashed and solid bands denote those before and after deformation, respectively.

Proportional loading is imposed on the edges of the layer, i.e.,

$$\frac{\varepsilon_x^0}{\varepsilon_z^0} = r = const, \quad \frac{\sigma_z^0}{\sigma^0} = \frac{2+r}{\sqrt{3(1+r+r^2)}}, \quad \frac{\sigma_x^0}{\sigma^0} = \frac{1+2r}{\sqrt{3(1+r+r^2)}}. \tag{C.1}$$

The equilibrium conditions across the band yield

$$\sigma_{nn}^0\bar{h}_0(t) = \sigma_{nn}\bar{h}(t), \quad \sigma_{nt}^0\bar{h}_0(t) = \sigma_{nt}\bar{h}(t), \quad \text{or} \quad \frac{\sigma_{nt}}{\sigma_{nn}} = \frac{\sigma_{nt}^0}{\sigma_{nn}^0}, \tag{C.2}$$

where $\sigma_{nn}^0$ and $\sigma_{nt}^0$ are the normal and shear stress components in the band. By combining the equilibrium condition and the definition of logarithmic strain, we have

$$\frac{\sigma_{nn}^0/\sigma^0}{\sigma_{nn}/\sigma} = (1-\xi)\frac{\sigma}{\sigma^0}\exp\left(\varepsilon_y - \varepsilon_y^0\right). \tag{C.3}$$

From the relation between the normal stress and the principle stress in the uniform section (Fig. C.1), we can obtain

$$\frac{\sigma_{nn}^0}{\sigma^0} = \frac{(2+r)\cos^2\gamma + (1+2r)\sin^2\gamma}{\sqrt{3(1+r+r^2)}}. \tag{C.4}$$

By applying the incompressibility condition ($\varepsilon_x^0 + \varepsilon_y^0 + \varepsilon_z^0 = 0$) and the definition of equivalent strain in the uniform section, the strain in the thickness dimension is

$$\varepsilon_y^0 = -\frac{\sqrt{3}(1+r)}{2\sqrt{1+r+r^2}}\varepsilon^0 = -C\varepsilon^0. \tag{C.5}$$

Assume

$$d\varepsilon_{tt} = d\varepsilon_{tt}^0, \tag{C.6}$$

and consider the law of plastic flow Eq. (14) as well as the equilibrium condition Eq. (C.2), we get

$$\frac{\sigma_{nn}}{\sigma} = \frac{1}{AH}\sqrt{1 - B\left(\frac{d\varepsilon^0}{d\varepsilon}\right)^2}, \tag{C.7}$$

$$A = \frac{\sqrt{3}}{2}, \quad B = \frac{3(\sin^2\gamma + r\cos^2\gamma)^2}{4(1+r+r^2)}, \quad H = \sqrt{1 + \left[\frac{2(r-1)\sin\gamma\cos\gamma}{(2+r)\cos^2\gamma + (1+2r)\sin^2\gamma}\right]^2}. \tag{C.8}$$

Substitute (C.4), (C.5) and (C.7) into the equilibrium condition (C.3), we have

$$H\sqrt{(1-B-G)}\left[1 - B\left(\frac{d\varepsilon^0}{d\varepsilon}\right)^2\right]^{-1/2} = (1-\xi)\frac{\sigma}{\sigma^0}\exp\left(C\varepsilon^0 + \varepsilon_y\right), \tag{C.9}$$

$$G = \frac{(r-1)^2\sin^2\gamma\cos^2\gamma}{(1+r+r^2)}. \tag{C.10}$$

From Eqs. (14), (C.6) and (C.7), we get

$$\frac{d\varepsilon_y}{d\varepsilon} = -\frac{A}{H}\left[1 - B\left(\frac{d\varepsilon^0}{d\varepsilon}\right)^2\right]^{1/2} - D\frac{d\varepsilon^0}{d\varepsilon}, \tag{C.11}$$

$$D = \frac{\sqrt{3}(\sin^2\gamma + r\cos^2\gamma)}{4\sqrt{(1+r+r^2)}}. \tag{C.12}$$

Eqs. (C.9) and (C.11) can be combined to calculate the equivalent strains $\varepsilon^0$ and $\varepsilon$. Note that if we set $\sigma = K\varepsilon^N$ (for power law hardening material), the above equations are identical to those given by Hutchinson and Neale (1978).

## Appendix D. Finite element simulations for gradient structure

In order to calculate the lateral surface non-uniform deformation as well as GNDs density and back stress, we use ABAQUS (2012) by constructing a 1/4 symmetric finite element model considering the geometric symmetry and the uniaxial load condition. The element is chosen to be four-node bilinear plane strain element CPE4. The detailed procedure is given as follows. (1) the limit strain $\varepsilon_{zi}^{0*}$ in the uniform section or the limit strain ration $\chi_i$ of free-standing layer $i$ ($i = 1, 2, ..., n+1$) is calculated using the M-K type analysis. (2) select a series of applied strain $\varepsilon_z^a$. (3) when the applied strain $\varepsilon_z^a$ is equal to the limit strain of layer $k$, $\varepsilon_{zk}^{0*}$, the z-component strains $\varepsilon_{zi}$ for each constituent layers of the gradient structure can be obtained using Eq. (13). (4) calculate the value of thermal expansion coefficient $\alpha_i$ for each layer by $\alpha_i = \varepsilon_{zi}/3$ (Eq. (17)). (5) obtain from the finite element simulations the lateral ($x$) displacement of the $j$-th node on the lateral surface along the sample depth $u_j$, $j = 1, 2, 3, ..., n^*+1$ ($n^*$ is the layer number of the whole sample in the finite element model), for the given applied strain. (6) calculate the lateral surface non-uniform deformation parameter a for layer $j-1$ by using $a_{j-1} = (u_j - u_{j-1})$, $j = 2, 3, ..., n^*+1$. (7) obtain parameter $a$ for another given applied strain by repeating procedures (3)–(6). (8) calculate the GNDs density $\rho_G$ (Eq. (6)) and the back stress $\sigma_b$ (Eq. (11)) as well as the flow stress of each layer subjected to uniaxial tension (Eq. (4)).

## Appendix E. Supplementary data

Supplementary data related to this article can be found at http://dx.doi.org/10.1016/j.ijplas.2016.10.003.

## References

ABAQUS, 2012. ABAQUS/Standard User's Manual Version 6, pp. 12—22.
Ashby, M., 1970. The deformation of plastically non-homogeneous materials. Philos. Mag. 21, 399—424.
Bayley, C.J., Brekelmans, W.A.M., Geers, M.G.D., 2006. A comparison of dislocation induced back stress formulations in strain gradient crystal plasticity. Int. J. Solids Struct. 43, 7268—7286.
Beyerlein, I.J., Demkowicz, M.J., Misra, A., Uberuaga, B.P., 2015. Defect-interface interactions. Prog. Mater. Sci. 74, 125—210.
Capolungo, L., Spearot, D.E., Cherkaoui, M., McDowell, D.L., Qu, J., Jacob, K.I., 2007. Dislocation nucleation from bicrystal interfaces and grain boundary ledges: relationship to nanocrystalline deformation. J. Mech. Phys. Solids 55, 2300—2327.
Carvalho Resende, T., Bouvier, S., Abed-Meraim, F., Balan, T., Sablin, S.S., 2013. Dislocation-based model for the prediction of the behavior of b.c.c. materials — grain size and strain path effects. Int. J. Plast. 47, 29—48.
Delince, M., Brechet, Y., Embury, J.D., Geers, M.G.D., Jacques, P.J., Pardoen, T., 2007. Structure-property optimization of ultrafine-grained dual-phase steels using a micro structure-based strain hardening model. Acta Mater 55, 2337—2350.
Demir, E., Raabe, D., Zaafarani, N., Zaefferer, S., 2009. Investigation of the indentation size effect through the measurement of the geometrically necessary dislocations beneath small indents of different depths using EBSD tomography. Acta Mater 57, 559—569.
Duhamel, C., Brechet, Y., Champion, Y., 2010. Activation volume and deviation from Cottrell-Stokes law at small grain size. Int. J. Plast. 26, 747—757.
Estrin, Y., Mecking, H., 1984. A unified phenomenological description of work-hardening and creep based on one-parameter models. Acta Metall. 32, 57—70.
Evers, L.P., Brekelmans, W.A.M., Geers, M.G.D., 2004. Scale dependent crystal plasticity framework with dislocation density and grain boundary effects. Int. J. Solids Struct. 41, 5209—5230.
Fang, T.H., Li, W.L., Tao, N.R., Lu, K., 2011. Revealing extraordinary intrinsic tensile plasticity in gradient nano-grained copper. Science 331, 1587—1590.
Farrokh, B., Khan, A.S., 2009. Grain size, strain rate, and temperature dependence of flow stress in ultra-fine grained and nanocrystalline Cu and Al: synthesis, experiment, and constitutive modeling. Int. J. Plast. 25, 715—732.
Fleck, N.A., Hutchinson, J.W., 1993. A phenomenological theory for strain gradient effects in plasticity. J. Mech. Phys. Solids 41, 1825—1857.
Gao, H., Huang, Y., Nix, W.D., Hutchinson, J.W., 1999. Mechanism-based strain gradient plasticity— I. Theory. J. Mech. Phys. Solids 47, 1239—1263.
Gleiter, H., 1989. Nanocrystalline materials. Prog. Mater. Sci. 33, 223—315.
Groma, I., Csikor, F.F., Zaiser, M., 2003. Spatial correlations and higher-order gradient terms in a continuum description of dislocation dynamics. Acta Mater 51, 1271—1281.
Huang, Y., Qu, S., Hwang, K.C., Li, M., Gao, H., 2004. A conventional theory of mechanism-based strain gradient plasticity. Int. J. Plast. 20, 753—782.
Hutchinson, J., Neale, K., 1978. Sheet necking-II. Time-independent behavior. In: Koistinen, D.P. (Ed.), Mechanics of Sheet Metal Forming. Plenum Press, New York, pp. 127—153.
Khan, A.S., Zhang, H.Y., Takacs, L., 2000. Mechanical response and modeling of fully compacted nanocrystalline iron and copper. Int. J. Plast. 16, 1459—1476.
Khan, A.S., Liu, J., 2016. A deformation mechanism based crystal plasticity model of ultrafine-grained/nanocrystalline FCC polycrystals. Int. J. Plast. 86, 56—69.
Kou, H., Lu, J., Li, Y., 2014. High-strength and high-ductility nanostructured and amorphous metallic materials. Adv. Mater 26, 5518—5524.
Li, J., Chen, S., Wu, X., Soh, A.K., Lu, J., 2010a. The main factor influencing the tensile properties of surface nano-crystallized graded materials. Mater. Sci. Eng. A 527, 7040—7044.
Li, J., Soh, A.K., 2012a. Enhanced ductility of surface nano-crystallized materials by modulating grain size gradient. Modell. Simul. Mater. Sci. Eng. 20, 085002.
Li, J., Soh, A.K., 2012b. Modeling of the plastic deformation of nanostructured materials with grain size gradient. Int. J. Plast. 39, 88—102.
Li, J., Chen, S., Wu, X., Soh, A.K., 2015a. A physical model revealing strong strain hardening in nano-grained metals induced by grain size gradient structure. Mater. Sci. Eng. A 620, 16—21.
Li, W., Yuan, F., Wu, X., 2015b. Atomistic tensile deformation mechanisms of Fe with gradient nano-grained structure. AIP Adv. 5, 087120.
Li, W.L., Tao, N.R., Lu, K., 2008. Fabrication of a gradient nano-micro-structured surface layer on bulk copper by means of a surface mechanical grinding treatment. Scr. Mater 59, 546—549.
Li, X.Y., Wei, Y.J., Lu, L., Lu, K., Gao, H.J., 2010b. Dislocation nucleation governed softening and maximum strength in nano-twinned metals. Nature 464, 877—880.
Li, Y.J., Raabe, D., Herbig, M., Choi, P.P., Goto, S., Kostka, A., Yarita, H., Borchers, C., Kirchheim, R., 2014. Segregation stabilizes nanocrystalline bulk steel with near theoretical strength. Phys. Rev. Lett. 113, 106104.
Li, Z., Pradeep, K.G., Deng, Y., Raabe, D., Tasan, C.C., 2016. Metastable high entropy dual phase alloys overcome the strength ductility trade off. Nature 534, 227—230.
Liu, H., Mishnaevsky Jr., L., 2014. Gradient ultrafine-grained titanium: computational study of mechanical and damage behavior. Acta Mater 71, 220—233.
Liu, J., Khan, A.S., Takacs, L., Meredith, C.S., 2015. Mechanical behavior of ultrafine-grained/nanocrystalline titanium synthesized by mechanical milling plus consolidation: experiments, modeling and simulation. Int. J. Plast. 64, 151—163.
Lu, K., Lu, J., 2004. Nanostructured surface layer on metallic materials induced by surface mechanical attrition treatment. Mat. Sci. Eng. A 375—377, 38—45.
Lu, K., 2014. Making strong nanomaterials ductile with gradients. Science 345, 1455—1456.
Lu, L., Chen, X., Huang, X., Lu, K., 2009. Revealing the maximum strength in nanotwinned copper. Science 323, 607—610.
Lyu, H., Ruimi, A., Zbib, H.M., 2015. A dislocation-based model for deformation and size effect in multi-phase steels. Int. J. Plast. 72, 44—59.
Ma, E., 2006. Eight routes to improve the tensile ductility of bulk nanostructured metals and alloys. JOM 58, 49—53.
Marciniak, Z., Kuczyński, K., Pokora, T., 1973. Influence of the plastic properties of a material on the forming limit diagram for sheet metal in tension. Int. J. Mech. Sci. 15, 789—800.
Martínez-Pañeda, E., Niordson, C.F., 2016. On fracture in finite strain gradient plasticity. Int. J. Plast. 80, 154—167.
Martínez-Pañeda, E., Niordson, C.F., Bardella, L., 2016. A finite element framework for distortion gradient plasticity with applications to bending of thin foils. Int. J. Solids Struct. 96, 288—299.
Meyers, M.A., Mishra, A., Benson, D.J., 2006. Mechanical properties of nanocrystalline materials. Prog. Mater. Sci. 51, 427—556.
Moering, J., Ma, X., Chen, G., Miao, P., Li, G., Qian, G., Mathaudhu, S., Zhu, Y., 2015. The role of shear strain on texture and microstructural gradients in low carbon steel processed by Surface Mechanical Attrition Treatment. Scr. Mater 108, 100—103.
Moering, J., Ma, X., Malkin, J., Yang, M., Zhu, Y., Mathaudhu, S., 2016. Synergetic strengthening far beyond rule of mixtures in gradient structured aluminum rod. Scr. Mater 122, 106—109.
Nairn, J.A., Mendels, D.-A., 2001. On the use of planar shear-lag methods for stress-transfer analysis of multilayered composites. Mech. Mater 33, 335—362.
Nielsen, K.L., Niordson, C.F., 2014. A numerical basis for strain-gradient plasticity theory: rate-independent and rate-dependent formulations. J. Mech. Phys. Solids 63, 113—127.
Ovid'ko, I., Langdon, T., 2012. Enhanced ductility of nanocrystalline and ultrafine-grained metals. Rev. Adv. Mater. Sci. 30, 103—111.
Ovid'ko, I.A., 2002. Materials science - deformation of nanostructures. Science 295, 2386—2386.

Rodríguez-Galán, D., Sabirov, I., Segurado, J., 2015. Temperature and stain rate effect on the deformation of nanostructured pure titanium. Int. J. Plast. 70, 191–205.

Rupert, T.J., 2016. The role of complexions in metallic nano-grain stability and deformation. Curr. Opin. Solid State Mater. Sci. http://dx.doi.org/10.1016/j.cossms.2016.05.005 in press.

Wang, Y.M., Chen, M.W., Zhou, F.H., Ma, E., 2002. High tensile ductility in a nanostructured metal. Nature 419, 912–915.

Wei, Y., Li, Y., Zhu, L., Liu, Y., Lei, X., Wang, G., Wu, Y., Mi, Z., Liu, J., Wang, H., 2014. Evading the strength–ductility trade-off dilemma in steel through gradient hierarchical nanotwins. Nat. Commun. 5, 3580.

Weng, G.J., 2011. A composite model of nanocrystalline materials. In: Li, J.C.M. (Ed.), Mechanical Properties of Nanocrystalline Materials. Pan Stanford Publishing, Hackensack, NJ, pp. 93–135.

Wu, X., Jiang, P., Chen, L., Yuan, F., Zhu, Y.T., 2014a. Extraordinary strain hardening by gradient structure. Proc. Natl. Acad. Sci. U. S. A. 111, 7197–7201.

Wu, X., Jiang, P., Chen, L., Zhang, J., Yuan, F., Zhu, Y., 2014b. Synergetic strengthening by gradient structure. Mater. Res. Lett. 2, 185–191.

Yang, M., Pan, Y., Yuan, F., Zhu, Y., Wu, X., 2016. Back stress strengthening and strain hardening in gradient structure. Mater. Res. Lett. 4, 145–151.

Yang, X., Ma, X., Moering, J., Zhou, H., Wang, W., Gong, Y., Tao, J., Zhu, Y., Zhu, X., 2015. Influence of gradient structure volume fraction on the mechanical properties of pure copper. Mater. Sci. Eng. A 645, 280–285.

Yefimov, S., Groma, I., van der Giessen, E., 2004. A comparison of a statistical-mechanics based plasticity model with discrete dislocation plasticity calculations. J. Mech. Phys. Solids 52, 279–300.

Yin, Z., Yang, X., Ma, X., Moering, J., Yang, J., Gong, Y., Zhu, Y., Zhu, X., 2016. Strength and ductility of gradient structured copper obtained by surface mechanical attrition treatment. Mater. Des. 105, 89–95.

Youssef, K.M., Scattergood, R.O., Murty, K.L., Horton, J.A., Koch, C.C., 2005. Ultrahigh strength and high ductility of bulk nanocrystalline copper. Appl. Phys. Lett. 87, 091904.

Yuan, F., Chen, P., Feng, Y., Jiang, P., Wu, X., 2016. Strain hardening behaviors and strain rate sensitivity of gradient-grained Fe under compression over a wide range of strain rates. Mech. Mater 95, 71–82.

Zeng, Z., Li, X., Xu, D., Lu, L., Gao, H., Zhu, T., 2016. Gradient plasticity in gradient nano-grained metals. Extr. Mech. Lett. http://dx.doi.org/10.1016/j.eml.2015.12.005 in press.

Zhao, Y.H., Topping, T., Bingert, J.F., Thornton, J.J., Dangelewicz, A.M., Li, Y., Liu, W., Zhu, Y.T., Zhou, Y.Z., Lavernia, E.L., 2008. High tensile ductility and strength in bulk nanostructured nickel. Adv. Mater 20, 3028–3033.

Zhu, T., Li, J., 2010. Ultra-strength materials. Prog. Mater. Sci. 55, 710–757.